

pubs.acs.org/journal/apchd5 Article

# On-Chip Single-Layer Integration of Diamond Spins with Microwave and Plasmonic Channels

Mikhail Y. Shalaginov,\* Simeon I. Bogdanov, Alexei S. Lagutchev, Alexander V. Kildishev, Alexandra Boltasseva, and Vladimir M. Shalaev



Cite This: ACS Photonics 2020, 7, 2018–2026



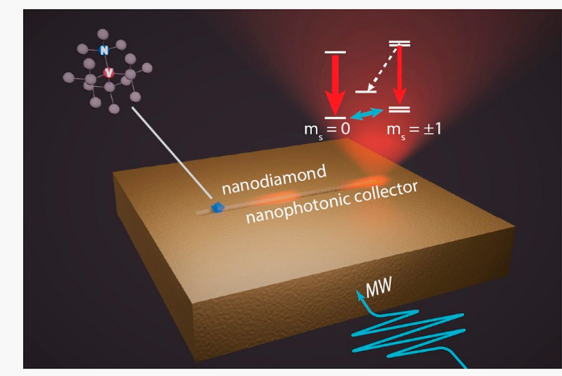
ACCESS

Metrics & More



Supporting Information

ABSTRACT: On-chip scalable integration represents a major challenge for practical quantum devices. One particular challenge is to implement on-chip optical readout of spins in diamond. This readout requires simultaneous application of optical and microwave fields along with the efficient collection of fluorescence. These requirements are typically met using bulk optical components and dedicated microwave lines. Here, we experimentally demonstrate an on-chip integrated interface for diamond nitrogen vacancy (NV) spin-state preparation and readout, implemented in a planar single layer with only one patterning step. A nanodiamond with NV centers is positioned inside a v-groove waveguide milled in a thick gold film. The gold film carries the microwave control signal, while the v-groove acts as a fluorescence collector and, potentially, as an integrated pump filter. Hence, the device dimensions and fabrication complexity are substantially reduced.



Our approach fosters further development of ultracompact nanoscale quantum sensors and quantum information processing devices on a monolithic platform.

KEYWORDS: quantum optical-microwave interface, nitrogen-vacancy centers, nanodiamond, plasmonic waveguide, optically detected magnetic resonance, spin readout

olor centers in solids are promising candidates for the development of integrated quantum devices. These defects possess unique optical and spin properties and are compatible with scalable on-chip technologies. Of particular interest are the quantum emitters realizing the so-called spinlight interfaces. Examples of such emitters include color centers in diamond,<sup>2</sup> silicon carbide,<sup>3</sup> rare-earth ions,<sup>4</sup> and donors in silicon.<sup>5</sup> The applications of the solid-state defects encompass large-scale quantum simulators and multifunctional nanoscale sensors, 7-10 however, all of their demonstrations to date involved bulky table-top setups. There is a strong need for further miniaturization of devices based on solid-state defects and their full integration on field-deployable platforms, such as semiconductor chips. The necessary components to be interfaced on-chip include pump sources, waveguides, the infrastructure for the control of electron spin states (e.g., microwave antennae and magnets), and photodetectors. Recently, several attempts have been made toward realization of CMOS-integrated quantum sensors with an out-of-plane multilayer architecture. <sup>11,12</sup> In our approach, we aim at constructing an in-plane single-layer interface, which simultaneously facilitates immediate exposure of color centers to the probed environment, immediate proximity to microwave lines, minimization of readout cross-talk between different sensors, and promises on-chip integration of the optical pump.

In this work, we utilize nitrogen-vacancy (NV) centers in diamonds, 13,14 best known for their exceptional electron spin coherence at room temperature 15 and above. 16 NV's fluorescence intensity is spin-dependent, and this dependence can be used for optical spin state readout. The probability of emitting a photon is dictated by the distribution of the center's ground-state population over the spin-triplet sublevels  $m_s = 0$ ,  $\pm 1$  (level diagram in Figure 1). Upon optical excitation, the NV center spontaneously decays to its ground orbital state following radiative or nonradiative paths. The nonradiative decay probability for the  $m_s = \pm 1$  spin projections is noticeably higher, resulting in a reduced fluorescence signal compared to the  $m_s = 0$  projection state. The relative difference in the fluorescence signals from these spin states is termed the spin contrast. The zero-field energy splitting between the  $m_s = 0$ and  $m_s = \pm 1$  orbital ground state sublevels is about 2.87 GHz.<sup>17</sup> Under constant optical excitation, the NV center is predominantly in the  $m_s = 0$  state. The NV  $m_s = 0 \rightarrow m_s = \pm 1$ 

Received: February 28, 2020 Published: July 20, 2020





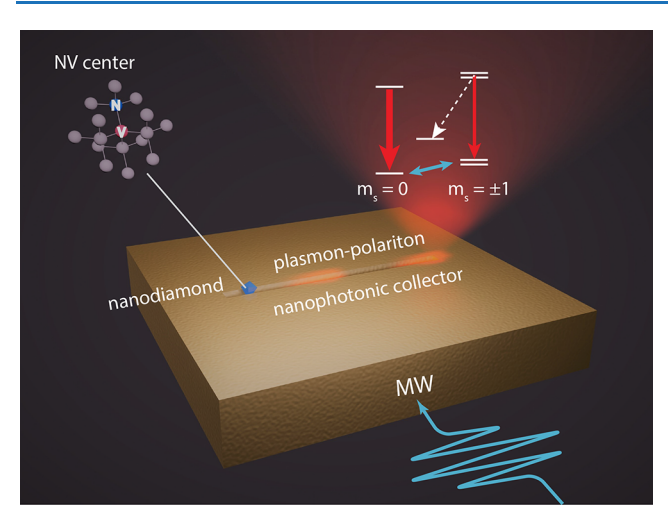


**Figure 1.** Artistic rendering of the microwave-spin-plasmon interface for future on-chip sensing and quantum information processing devices. The interface consists of a nanodiamond nitrogen-vacancy ensemble (NVE) coupled to a v-groove nanophotonic collector milled in a thick gold film. The NVE fluorescence is channeled into the collector and then is outcoupled into the far field. The gold film simultaneously acts as a carrier for the microwave excitation.

transitions can then be probed by applying an AC magnetic field at different frequencies and monitoring the fluorescence brightness. As the microwave (MW) frequency is swept over the spin transition frequency, the  $m_{\rm s}=\pm 1$  state becomes more populated and the brightness of the NV decreases. The observable electron spin resonance lies at the heart of multifunctional nanoscale sensing capability.  $^{18,19}$  In addition, control of the electron spin resonance is essential for applications harnessing nearby nuclear spins.  $^{20-23}$ 

The sensing capabilities of NV centers rely on the readout of the NV spin population as a function of the external electromagnetic, 24,25 strain, 26,27 or temperature fields. 28,29 Several schemes for NV spin readout have been demonstrated in the past. 13,30-35 The fluorescence-based readout (later termed as optically detected magnetic resonance or ODMR) remains particularly advantageous due to its simplicity and room-temperature operation. The sensitivity of the spinpopulation measurement in this scheme depends on the detected photon rate, as well as on the achieved maximum spin contrast between the  $m_s = 0$  and  $m_s = \pm 1$  spin states. One can increase the detected photon rate by enhancing the fluorescence rate  $\gamma$ , employing a larger number of NVs, or improving the photon collection efficiency. In this paper, we exploited nitrogen-vacancy ensembles (NVEs) rather than single NVs. NVEs yield a stronger fluorescence signal and could find practical applications in most sensing schemes. In our prior work, we found that spin readout in dense NVEs is compromised in the optical saturation regime.<sup>36</sup> To overcome this issue, one has to operate in the weak excitation regime, in which the spin contrast is roughly inversely proportional to the emission rate  $\gamma$ . Therefore, rather than attempting to enhance  $\gamma$ , the spin readout sensitivity in NVEs can instead be improved via an efficient photon collection scheme. A suitable integrated fluorescence collecting structure for NVE spin readout is a waveguide featuring a high collection efficiency ( $\beta$ -factor), but a moderate enhancement of  $\gamma$ . So far, those conditions have been achieved in several architectures, including diamond

nanobeams, <sup>31,37</sup> dielectric-loaded plasmonic waveguides, <sup>38</sup> and channel plasmonic waveguides. <sup>39</sup>

As of now, a few works have indicated the possible routes toward on-chip interface combining color-center spins, optical collectors/waveguides, and microwave delivery channels. 37,40,41 Here we present a different approach toward concurrent onchip integration of optical and MW channels for NV spin manipulation and readout. Plasmon-polaritons, particularly channel plasmon-polaritons, offer more compact architectures with better integration prospects, as well as additional functionalities. 42,43 The conducting properties of such metallic structures enable several important features, including NV charge state control by applied voltage, 44,45 as well as precise and fast placing of nanodiamonds via induced electrothermoplasmonic effect. 46 Prior to our work, Al-Baiaty et al. have demonstrated NV spin readout via surface plasmonpolaritons propagating along the chemically synthesized silver nanowires. 47 However, nanowires are not integration friendly and feature low coupling efficiency. Among various plasmonic couplers, v-groove channels are more suitable for scalable onchip integration and can collect more efficiently the fluorescence from nanodiamond-based NVs. 48 Here, we experimentally verified that NV spin readout can be achieved by collecting the fluorescence signal from the end of a v-groove channel.

## ■ CONCEPT OF ON-CHIP MICROWAVE-SPIN-PLASMON INTERFACE

In ODMR experiments, it is essential to deliver both optical and microwave excitations as well as to collect the spindependent fluorescence. The delivery of the microwave excitation is usually performed using a dedicated conductor, separated from the optical pumping and fluorescence collection channels.<sup>37,47</sup> Combined integration of MW and optical infrastructures can be achieved on a single conducting platform. A thick metal film patterned with nanophotonic collector-waveguides can simultaneously deliver the MW control signal, couple the NV fluorescence into channel plasmon-polaritons<sup>45</sup> (referred to as plasmons later in the text), and partially prevent the residual pump to be coupled into the collector. In this work, we present the first experimental demonstration of an on-chip microwave spinplasmon interface. The interface consists of an NV ensemble (NVE) coupled to a gold v-groove nanophotonic collector (Figure 1). We numerically simulated the coupling of the NVE to a plasmonic mode (Figure 2) and characterized the optical properties of the coupled NVE (Figure 3). We detected the spin resonance by exciting the spins through the microwaves supported by the gold film and collecting the fluorescence into the v-groove (Figure 4).

#### RESULTS

**Design of a Fluorescence Collector with High Coupling Efficiency.** We performed 3D numerical simulations of the NVE coupled to the v-groove (Figure 2a) and found that the groove geometry simultaneously satisfies the conditions of high coupling efficiency and moderate emission rate enhancement. The nanodiamonds used in the experiment contained approximately 400 NVs on average. The response of the NVs is expected to vary depending on each NV's location and dipole orientation. The electric field of the v-groove fundamental mode is primarily directed along *x*-axis,

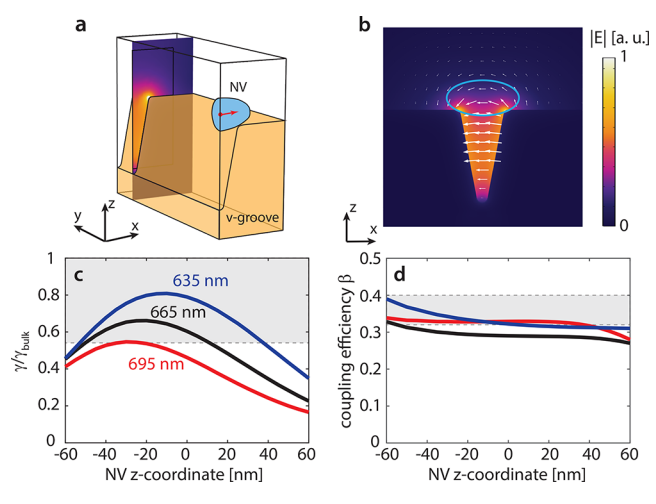


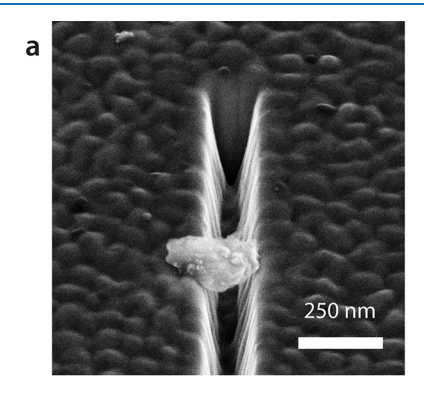
Figure 2. Numerical simulations of the NV ensemble coupled to the nanophotonic collector: (a) Electric field cross-section at a distance of 750 nm from the NV. The simulation domain contains a gold v-groove and an NV as a dipolar emitter (red dot) embedded into a diamond ellipsoid. (b) Distribution of electric field magnitude corresponding to a fundamental channel plasmon mode excited in the v-groove, obtained from 2D eigenmode analysis. (c) Simulated total decay rate  $\gamma$  normalized to the intrinsic rate of an NV inside a bulk diamond ( $\gamma_{\text{bulk}} = 12.8^{-1} \text{ ns}^{-1}$ ). (d) Simulated coupling efficiency  $\beta$  (into both collector directions) vs emitter vertical position inside a nanodiamond (z = 0 aligns with the nanodiamond center). Gray areas on (c) and (d) cover the range of experimentally obtained values.

perpendicular to the groove edges. Therefore, the strongest contribution to the collected fluorescence is expected from the x-oriented dipoles. Additionally, the E-field distribution of the fundamental plasmonic mode (Figure 2b) suggests that the strongest variation of dipole response is expected in the z direction. We simulated the response of x-oriented dipoles depending on their location along the z-axis, choosing the origin z = 0 to coincide with the nanodiamond's center (Figure 2a). The calculated total decay rate values were normalized to the decay rate in bulk diamond<sup>50</sup> (12.8<sup>-1</sup> ns<sup>-1</sup>) and span from 0.23 to 0.66, at the NVE peak emission wavelength of 665 nm (see Figure 2c, black curve). All the NV centers in the ensemble coupled to the v-groove were therefore expected to be subradiant with respect to NV centers in bulk diamond, thus, favoring sensitive spin readout in the weak excitation regime.

The coupling efficiency of the NVE to a propagating plasmonic mode was estimated by integrating the power density in the zx-plane at a distance  $v_0 = 0.75 \mu m$  away from the nanodiamond center (see cross-section plane in Figure 2a). The integrated power was divided by the propagation loss factor  $(\exp(-y_0/L_p) \sim 0.8)$  of the fundamental plasmonic mode Figure 2b), with  $L_p = 3.14 \mu m$  being the propagation length at 665 nm. As a result, the  $\beta$ -factor was found to be around 0.3 (see Methods, Numerical Simulations), almost independently of the NV's position along the z-axis (Figure 2d, black curve). Additionally, we obtained numerical values for  $\beta$ and  $\gamma$  at 635 and 695 nm (Figure 2c,d; red and blue curves), which correspond to the red and blue edges of the NVE emission spectrum at half-maximum level, respectively (see Figure S2a, Supporting Information). The coupling efficiency in the NV-groove geometry depends weakly on both the NV position inside nanodiamond and its emission wavelength, thereby facilitating the interpretation of the experimental results.

Experimental Measurements of Fluorescence Lifetime and Coupling Efficiency. We fabricated a microwavespin-plasmon interface by milling v-grooves in a 380 nm thick gold film and depositing nanodiamonds on the surface of the sample (see Methods, Sample Fabrication). An SEM image of a nanodiamond coupled to the v-groove is shown in Figure 3a. The NVE fluorescence decay was measured by using a timecorrelated single-photon counting method and the data was fitted with a gamma-weighted integral of exponential functions convolved with the instrument response function (Figure 3b).<sup>36</sup> The fitting-retrieved averaged lifetime was  $\tau_{av} = 16.2$  ns  $(\gamma_{\rm exp}/\gamma_{\rm bulk} = 0.79)$  and lifetime dispersion  $\delta \tau = 10.5$  ns  $(\delta \gamma/\gamma_{\rm bulk})$ = 0.5). The range of experimental fluorescence lifetime values was visually marked by the gray area in Figure 2c. Experimental decay rates are slightly faster than the theoretically predicted ones, the discrepancy being most likely due to the contribution of nonradiative decay paths in nanodiamond-based NVs. 51

Measurement of NVE Electron-Spin Resonance through the Channel Plasmons. The coupling efficiency into the collector was measured by analyzing optical signals scattered from the groove ends (A, B) and emitted from the nanodiamond position (C), see Figure 4a. The nanodiamond was located at distances of  $l_{\rm A}=0.85\pm0.03~\mu{\rm m}$  and  $l_{\rm B}=9.85\pm0.03~\mu{\rm m}$  from A and B. Figure 4b shows distinct fluorescence spots corresponding to A, B, and C, obtained on the CCD camera upon exciting the NVE with a 532 nm focused laser



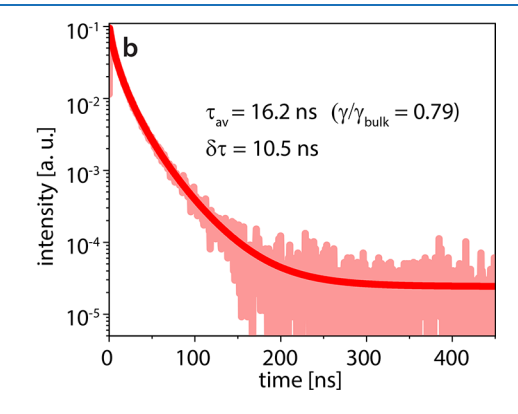


Figure 3. Nanodiamond inside a v-groove waveguide collector: (a) SEM image of the nanodiamond coupled to a gold v-groove. (b) Fluorescence decay curve fitted with the gamma-distributed sum of exponential decays, average lifetime  $\tau_{av}$  of 16.2 ns (or  $\gamma/\gamma_{bulk,exp} = 0.79$ ) with a dispersion  $\delta\tau$  of 10.5 ns.

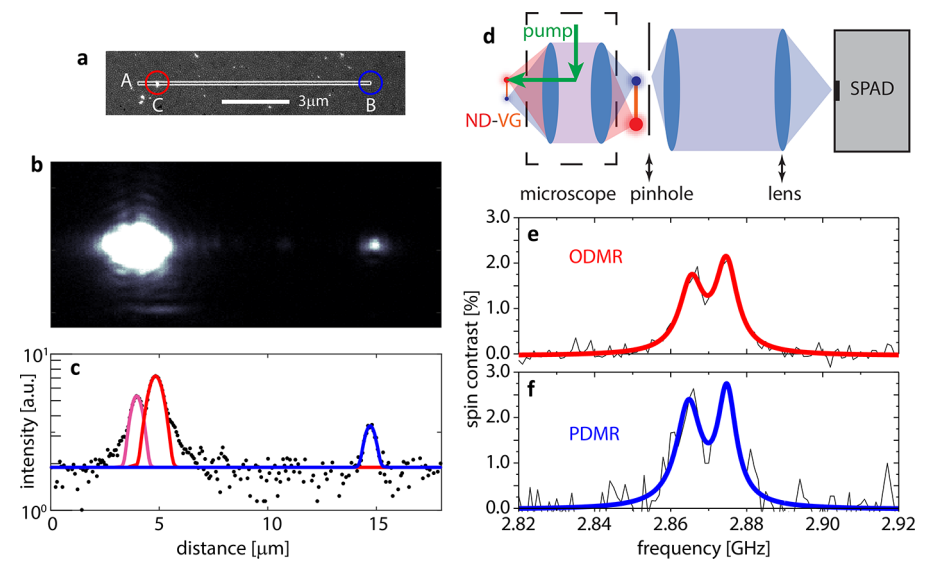


Figure 4. NV electron spin readout via plasmons. (a) SEM scan of the gold v-groove collector,  $10.7 \mu m$  long with the nanodiamond (ND) outlined with a red circle. The distances between the nanodiamond and the v-groove (VG) ends are  $0.85 \mu m$  (A) and  $9.85 \mu m$  (B). (b) Photoluminescence image obtained with a CCD camera depicts merged fluorescence spots at A and C, and fainter fluorescence scattering from B. (c) Profile cut of the CCD image along the propagation direction with Gaussian fits of the maxima at A, B, and C. (d) Schematic of the experimental method for collecting the fluorescence signal from B by adjusting the pinhole of the confocal microscope. (e and f) The spin-resonance curves measured using fluorescence from spots C (optically detected magnetic resonance) and B (plasmonically detected magnetic resonance), respectively.

beam. The brighter spot consisted of two partially overlapping peaks formed by direct emission from nanodiamond and plasmons scattered from the A end (red and pink peaks on Figure 4c). The fainter spot corresponded to plasmon scattering at point B. The fluorescence intensity at B was affected by the propagation losses (transmittance  $\sim$ 0.05) and a finite NV-to-plasmon coupling ( $\sim$ 0.2 in a single direction). Relative emission powers at A, B, and C spots were retrieved from integrating pixel counts over the areas of deconvolved peaks. We assumed that collection efficiency is the same for the considered spots A, B, and C. Plasmon propagation length  $L_{\rm p}$  and NVE-groove coupling efficiency  $\beta$  were calculated as

$$L_{\rm p} = (l_{\rm B} - l_{\rm A})/\ln(P_{\rm A}/P_{\rm B}) \approx 3.3 \pm 0.1 \ \mu \text{m}$$
 (1)

$$\beta = (P_{\rm A}e^{l_{\rm A}/L_{\rm P}} + P_{\rm B}e^{l_{\rm B}/L_{\rm P}})/(P_{\rm A}e^{l_{\rm A}/L_{\rm P}} + P_{\rm B}e^{l_{\rm B}/L_{\rm P}} + P_{\rm C}) \approx 0.36 \pm 0.04$$
(2)

The experimentally measured range of  $\beta$  values was grayed out in Figure 2d. Hence, we experimentally verified that the groove-coupled NVE offers a coupling efficiency of nearly 40% into the collector modes, which is in good agreement with the simulated results.

After characterizing the NVE fluorescence, we aimed at measuring the spin resonance of the NVE. Specifically, we measured the electron spin resonance by applying MW fields and detecting the fluorescence. The optical, microwave and detection channels were configured to follow a periodic sequence described in Methods (see also Figure S3a in Supporting Information). The spin resonance experiments were performed at zero magnetic field by sweeping the MW frequency between 2.82 and 2.92 GHz, and analyzing changes in fluorescence from points C (ODMR) and B (plasmonically detected magnetic resonance, PDMR, see Figure 4e,f). Importantly, the MW excitation was delivered directly through the groove-patterned gold film. Such a metal-based design significantly simplifies fabrication, shrinks the device footprint, and allows delivery of MW excitation over a large area. The

NVE optical transitions were induced by a 532 nm laser at a power of 15  $\mu$ W, which corresponds to excitation rates well below the saturation regime (see Figure S2b, Supporting Information). PDMR was measured by collecting the fluorescence scattered from the waveguide end B, while continuing to excite the NVE optically. For this purpose, we kept the excitation laser aligned on the nanodiamond and adjusted the pinhole and detector lens position in our homemade confocal microscope setup (see Figure 4d). Both ODMR and PDMR signals exhibited a double peak structure with a 10 MHz interpeak splitting, indicating presence of local strain in the nanocrystal. The two spectra are almost identical, but the PDMR method yields about 25% higher contrast. This increased spin contrast may be due to partial filtering of the fluorescence from NV neutral charge state (NV<sup>0</sup>), which is blue-shifted compared to NV<sup>-</sup> and features no spin contrast.

The estimated single-shot spin-readout SNR and magnetic field sensitivity of the fabricated interface are on the order of 0.01 and 100  $\mu T/Hz^{1/2}$ . These characteristics can be further improved by reducing losses in the collector, for instance, by shortening its length. Based on our numerical simulations, 1- $\mu$ m-long v-groove will have optical losses of 27%. In order to further reduce these losses, the nanophotonic collector can be fabricated from an epitaxial silver with an order of magnitude lower optical losses. The collector can be then adiabatically tapered into a low-loss photonic waveguide  $^{53,54}$  or directly coupled to a local integrated detector.  $^{55,56}$ 

#### DISCUSSION

On-chip integration is the key factor for enabling highefficiency, small footprint NV-centers-based quantum devices. Fabrication complexity and incompatibility with conventional manufacturing techniques are major stumbling blocks in achieving this goal. 40,57 In our work, we proposed and demonstrated an alternative metal-based single-layer platform for on-chip integration of color centers with optical and MW

channels. More specifically, we implemented concurrent onchip integration of optical and MW channels for NV spin manipulation and readout in a single material layer with a single patterning step as well as color-center spin readout via channel plasmons. In addition, we proposed and numerically studied a micron-scale pump filter with broadband transmittance naturally embedded into the system and realized a nonresonant structure for delivering uniform MW field over a centimeter-scale area. This on-chip integrated microwave-spinplasmon interface has the potential to advance the development of quantum sensors and quantum information processing devices. We envision that our compact interfaces can be applied in cytometry<sup>58</sup> and magnetic imaging.<sup>59</sup> The proposed approach could enable compact, submicrometer-scale footprints, higher operational speeds, and reduced fabrication complexity.

Conventionally, MW lines are independently integrated along with the photonic resonators as separate elements. Such device architectures require either multistep patterning on the same substrate with intermediate alignments, <sup>57</sup> or lithography on separate substrates with their subsequent hybridization. <sup>40</sup> In contrast, our interface significantly reduces fabrication complexity, since it can be implemented with a single patterning cycle.

For recording spatially varying magnetic fields, that is, wide field imaging, 60 there is a need for developing a platform featuring spatially distributed NV centers, which can be simultaneously and uniformly excited by optical and MW fields. Previously, the on-chip MW excitation over relatively large area was achieved by constructing resonant antennae encompassing NVEs, such as a double split-ring resonator<sup>61</sup> and inductor.<sup>11</sup> In both approaches, the magnetic field deviations were within 5% over the distances of 1 mm and 50  $\mu$ m, respectively. Here, we utilize a nonresonant structure for delivering MW excitation, where nanodiamonds are brought in direct contact with the metal film that carries the MW signal. The field has a nearly linear gradient of about  $\pm 5\%$ over a 1 mm distance, which is comparable to the state of the art. Our experiments showed the promise to deliver microwave signal over a cm-scale area without fabricating resonant structures and, therefore, without compromising the RF bandwidth.

In most scenarios involving nonresonant optical pumping, it is important to suppress the residual pump power with, for example, an optical filter. Additional Bragg grating filters can be introduced to perform pump filtering. 62 A waveguide-coupled excitation filter tailored for the NV center fluorescence spectrum (Figure S5a) has not yet been demonstrated. Here we proposed and numerically studied a collector-coupled excitation filter, which is naturally embedded into the system. Our nanophotonic collector, through its unique dispersion characteristics, offers a high transmission in the required broad spectral window, while strongly attenuating the pump at 532 nm. Additionally, the v-groove partially attenuates the unwanted NV $^0$  fluorescence. At 1  $\mu$ m propagation distance, the plasmonic waveguide filter provides a pump extinction of about 20 dB relative to the NV- fluorescence. Better filtering performance can be achieved by optimizing the v-groove geometry as well as by selecting a different metallic material and/or pump wavelength.

To further advance device prototyping, the proposed nanodiamond drop-casting method can be replaced by the hybrid electrothermoplasmonic nanotweezer (HENT) techni-

que, that promises faster and more precise placement of nanodiamonds into plasmonic waveguides. The HENT microfluidic dragging force appears due to a synergy between localized thermal gradients of plasmonic hotspots and externally applied AC electric fields. Hence, the interface layout comprised of a groove-patterned gold film is a particularly suitable configuration for implementing the HENT technique. Additionally, the precharacterized nanodiamonds can be controllably positioned inside the nanophotonic collectors by utilizing AFM-based pick-and-place techniques. <sup>63,64</sup>

The metallic film employed in our experiments carries both optical/plasmonic and microwave signals as well as a DC voltage bias. Thus, this approach is suited for stabilizing the negative NV<sup>-</sup> charge states. Band bending induced by the potential difference across a nanodiamond can stabilize the negative NV<sup>-</sup> charge state. This control of the charge state is expected to increase both PDMR contrast magnitude and signal-to-noise ratio, leading to improved spin-based sensing protocols. Additional enhancement of NVE spin-induced plasmonic readout SNR by order of magnitude can be attained by utilizing the spin-to-charge state conversion and charge-state detection protocols. 65,66

Another opportunity resides in realizing a low-temperature spin-plasmon chiral interface by employing spin-momentum locking of plasmons. For instance, circularly polarized optical transitions in NV centers or other atom-like systems can be mapped to the plasmon propagation momentum. This functionality can enable on-chip spin-induced emission routing and further exploration of novel chiral quantum architectures.

#### METHODS

Numerical Simulations. Eigenmode 2D analysis (COM-SOL 5.3a, Waves and Optics Module) was performed to investigate the fundamental v-groove mode parameters: field distribution, propagation length, and mode index. The simulation domain was a square box with an area of  $1 \times 1$  $\mu$ m<sup>2</sup>. Scattering boundary conditions were applied on its edges, and the wavelength was fixed to 665 nm, corresponding to the maximum of the NV emission spectrum. The groove's geometrical parameters included the opening angle of 21.6°, width of 160 nm, depth of 338 nm, radius of curvature at the bottom edge of 20 nm, and the radius of curvature at the side edges, 15 nm. These parameters were extracted from the SEM measurements of the fabricated v-grooves. Gold dielectric permittivity at the wavelength of 665 nm was  $\varepsilon = -12.35 +$ 1.05i, as obtained from the film's variable-angle spectroscopic ellipsometry characterization (J.A. Woollam Co.; W-VASE). The supported fundamental mode index was  $n_{VG} = 1.17 +$ 0.017*i*, corresponding to the propagation length  $L_{\rm P}$  of 3.14  $\mu$ m and the mode area  $A_{\rm M}$  of about 0.05  $\mu {\rm m}^2$ .

3D full-wave simulations were used to estimate the total decay rate  $\gamma$  and collection efficiency  $\beta$ . The computational domain size was a box with dimensions  $1.8 \times 0.6 \times 0.85 \ \mu \text{m}^3$  (length  $\times$  width  $\times$  height). The domain was surrounded by a perfectly matched layer (PML) shell with a thickness of 300 nm in order to suppress reflection from the boundaries. The nanodiamond was modeled as an ellipsoid with principal semiaxes of a=135 nm, b=c=65 nm. As a result of the ellipsoid reposing on the v-groove edges, the nanodiamond's center was elevated with respect to the gold—air planar interface by  $\sim$ 50 nm. The choice of nanodiamond shapes and sizes was based on the obtained SEM images of the

nanodiamond-groove system. An NV center was modeled as a volume current density oscillating coherently inside a 1 nm radius sphere serving as a dipole emitter. The electric dipole orientation was chosen along the E-field of v-groove fundamental mode. Due to symmetry considerations, we partitioned the computational domain into four subdomains and performed simulations on one of them.

The total decay rate was assumed to be proportional to the total power P dissipated by the dipole. The decay rate enhancement was computed as  $\gamma/\gamma_{\text{bulk}} = P/P_{\text{bulk}}$ , where  $\gamma_{\text{bulk}}$ and  $P_{\text{bulk}}$  are the reference quantities of an NV in bulk diamond. P<sub>bulk</sub>, the power emitted by a dipole inside diamond environment, was analytically estimated with a standard formula:  $^{70}$   $P_{\text{bulk}} = n_{\text{diam}} \omega_0^4 p^2 / (12\pi \epsilon_0 c^3)$ , where p is the dipole moment,  $n_{\mathrm{diam}}$  is the diamond refractive index, and  $\omega_0$  is the emission angular frequency. P was retrieved from NV-groove numerical simulations as a surface integral of power flow S through a 3 nm radius spherical surface encapsulating the emitting dipole and situated entirely within the nanodiamond volume  $P = \int_{ND} \mathbf{S} \cdot d\mathbf{A}$ . The NV-groove β-factor was calculated as  $\beta = P_{VG}/P$ , where  $P_{VG}$  is the power emitted into the vgroove modes propagating in both directions,  $P_{VG}$  =  $2e^{l/L_{\rm P}}\int_{A_{\rm CS}}$ **S**·d**A**.  $A_{\rm CS}$  is a rectangular cross-section area 0.8  $\times$ 1.04  $\mu$ m<sup>2</sup> positioned at a longitudinal distance  $l = 0.75 \mu$ m from the NV center.  $L_p = 3.14 \,\mu\text{m}$  is the propagation length of the v-groove fundamental mode that was obtained from 2D mode simulations. We strived to make the distance l as long as possible in order to minimize contributions of the emitted power, which reaches the collection area  $A_{CS}$  directly, without coupling to the v-groove fundamental mode. At the same time, we must respect a certain distance from  $A_{CS}$  to the PML layer in order to reduce potential numerical errors introduced by the PML boundary. In our simulation, the distance between the dipole and  $A_{CS}$  is limited by the maximum computable size of the simulation domain.

**Sample Fabrication.** A  $1 \times 1~{\rm cm}^2$  Si substrate was cleaned with a stripper Nano-Strip 2X, Cyantek (mixture of sulfuric and peroxymonosulfuric acids, hydrogen peroxide, and water) for 10 min, then rinsed with deionized water, and dried with nitrogen. Deposition was performed using an e-beam evaporator, operating at a base pressure of  $5 \times 10^{-7}$  Torr. To improve the adhesion, we introduced a 5 nm-thick Ti wetting layer. A 380-nm-thick gold film was deposited at a rate of 2 Å/s and its thickness was characterized by profilometry measurement.

We milled 18 channel v-grooves by bombarding the gold film with a focused  $Ga^+$  beam (Nova 200, FEI). The milling was performed under 30 kV accelerating voltage, with a current of 10 pA, magnification of approximately 20k. The size of a single-shot hole was measured to be 35 nm. The stream-file-based patterning was performed in a single loop with a dwell time of 150  $\mu$ s per dot and a pitch (distance between adjacent dots) of 3 nm. The milling was conducted in a random sequence in order to suppress material redeposition.

The dimensions of fabricated v-grooves were obtained from SEM: a length of  $10.70 \pm 0.05~\mu m$  and a separation distance (between v-grooves) of 5  $\mu m$ . Additionally, from a FIB-cut cross-section of a similar v-groove, the following dimensions were measured: a groove depth of  $340 \pm 10$  nm, an angle of  $21.6 \pm 0.5^{\circ}$ , and a width of  $160 \pm 10$  nm.

Nanodiamonds with an average size of 100 nm and containing nominally an average of 400 NVs (Adamas

Nano) were dropcast onto the patterned metal surface. During the dropcasting procedure, we dissolved the initial solution (1 mg/mL) 1000 times. A droplet of 10  $\mu$ L was deposited onto the sample, covered with a glass coverslip substrate for 1 min. The sample was then rinsed with DI water. Before depositing nanodiamonds the patterned gold film was covered with a poly allyalamine hydrochloride (PAH) layer to improve adhesion of individual nanocrystals to the gold surface. Using SEM imaging we found that that several nanodiamonds were placed into or very close to v-groove.

**NVE Optical Characterization.** The optical signals were collected and analyzed using a custom-made confocal microscope setup based on a Nikon Ti—U microscope body and equipped with a Nikon air objective (NA 0.9), a PI-561 objective piezo-stage driven by a E-712 controller (Physik Instrumente), a 532 nm CW laser (SLOC, GL532NA-200), a 514 nm picosecond laser (BDL-514-SMNi, Becker & Hickl), SPAD detector (SPCM-AQRH, Excelitas), an optical spectrometer (Ocean Optics QE65000), and a CCD camera (ATIK 414EX). The pump reflection was filtered by a longpass 550 nm filter with OD6. Microwaves were generated by an Agilent E8254A generator, modulated by a MiniCircuits ZASW-2–50DR+ switch, and amplified with 16 W MiniCircuits ZHL-16W-43 RF amplifier. The cable from the MW amplifier was soldered onto the sample's 380 nm thick gold film.

#### ASSOCIATED CONTENT

### Supporting Information

The Supporting Information is available free of charge at https://pubs.acs.org/doi/10.1021/acsphotonics.0c00325.

Optical properties of NV ensembles in a nanodiamond; Protocol of spin-resonance measurement; Numerical simulations of microwave field distribution and plasmonic waveguide transmittance (PDF)

#### AUTHOR INFORMATION

#### **Corresponding Author**

Mikhail Y. Shalaginov — School of Electrical and Computer Engineering, Birck Nanotechnology Center, and Purdue Quantum Science and Engineering Institute, Purdue University, West Lafayette, Indiana 47907, United States; orcid.org/0000-0002-1251-7766; Email: shalaginov@purdue.edu

#### Authors

Simeon I. Bogdanov — School of Electrical and Computer Engineering, Birck Nanotechnology Center, and Purdue Quantum Science and Engineering Institute, Purdue University, West Lafayette, Indiana 47907, United States; ◎ orcid.org/ 0000-0001-5608-546X

Alexei S. Lagutchev — School of Electrical and Computer Engineering, Birck Nanotechnology Center, and Purdue Quantum Science and Engineering Institute, Purdue University, West Lafayette, Indiana 47907, United States

Alexander V. Kildishev — School of Electrical and Computer Engineering, Birck Nanotechnology Center, and Purdue Quantum Science and Engineering Institute, Purdue University, West Lafayette, Indiana 47907, United States; orcid.org/0000-0002-8382-8422

Alexandra Boltasseva — School of Electrical and Computer Engineering, Birck Nanotechnology Center, and Purdue

Quantum Science and Engineering Institute, Purdue University, West Lafayette, Indiana 47907, United States

Vladimir M. Shalaev — School of Electrical and Computer Engineering, Birck Nanotechnology Center, and Purdue Quantum Science and Engineering Institute, Purdue University, West Lafayette, Indiana 47907, United States

Complete contact information is available at: https://pubs.acs.org/10.1021/acsphotonics.0c00325

#### **Author Contributions**

M.Y.S. and S.I.B. conceived the project. M.Y.S. and A.V.K. carried out the numerical simulations. M.Y.S. performed sample fabrication and characterization. S.I.B., M.Y.S., and A.S.L. built the optical experimental setup for measuring plasmonically detected magnetic resonance and photoluminescence characterization. M.Y.S. and S.I.B. collected and analyzed experimental data. A.V.K., A.B., and V.M.S. supervised the project. All authors discussed results and contributed to the writing of the manuscript.

#### Notes

The authors declare no competing financial interest.

#### ACKNOWLEDGMENTS

The authors acknowledge R. Cui and S. Choudhury for the help with v-groove fabrication and A. V. Akimov, V. V. Vorobyov for useful discussions. We additionally would like to thank S. Peana for help with manuscript preparation. This work was partially supported by the U.S. Department of Energy, Office of Basic Energy Sciences, Division of Materials Sciences and Engineering under Award DE-SC0017717 (S.I.B.), the National Science Foundation (NSF) ECCS Award 2015025, and the Office of Naval Research (ONR) DURIP Grant N00014-16-1-2767 (equipment grant used to purchase the scanning confocal microscope, lasers, and detectors used in this work). A.V.K. acknowledges the DARPA/DSO Extreme Optics and Imaging (EXTREME) Program, Award HR00111720032 (numerical modelling and simulations).

#### **■ REFERENCES**

- (1) Awschalom, D. D.; Hanson, R.; Wrachtrup, J.; Zhou, B. B. Quantum Technologies with Optically Interfaced Solid-State Spins. *Nat. Photonics* **2018**, *12* (9), 516–527.
- (2) Aharonovich, I.; Neu, E. Diamond Nanophotonics. *Adv. Opt. Mater.* **2014**, 2 (10), 911–928.
- (3) Kolesov, R.; Xia, K.; Reuter, R.; Stöhr, R.; Zappe, A.; Meijer, J.; Hemmer, P. R.; Wrachtrup, J. Optical Detection of a Single Rare-Earth Ion in a Crystal. *Nat. Commun.* **2012**, *3*, 1029.
- (4) Thiel, C. W.; Böttger, T.; Cone, R. L. Rare-Earth-Doped Materials for Applications in Quantum Information Storage and Signal Processing. *J. Lumin.* **2011**, *131* (3), 353–361.
- (5) Morse, K. J.; Abraham, R. J. S.; DeAbreu, A.; Bowness, C.; Richards, T. S.; Riemann, H.; Abrosimov, N. V.; Becker, P.; Pohl, H.-J.; Thewalt, M. L. W.; Simmons, S. A Photonic Platform for Donor Spin Qubits in Silicon. *Sci. Adv.* **2017**, *3* (7), e1700930.
- (6) Cai, J.; Retzker, A.; Jelezko, F.; Plenio, M. B. A Large-Scale Quantum Simulator on a Diamond Surface at Room Temperature. *Nat. Phys.* **2013**, *9* (3), 168–173.
- (7) Rendler, T.; Neburkova, J.; Zemek, O.; Kotek, J.; Zappe, A.; Chu, Z.; Cigler, P.; Wrachtrup, J. Optical Imaging of Localized Chemical Events Using Programmable Diamond Quantum Nanosensors. *Nat. Commun.* **2017**, *8*, 14701.
- (8) Degen, C. L.; Reinhard, F.; Cappellaro, P. Quantum Sensing. *Rev. Mod. Phys.* **2017**, *89* (3), 1–39.

- (9) Thiel, L.; Wang, Z.; Tschudin, M. A.; Rohner, D.; Gutiérrez-Lezama, I.; Ubrig, N.; Gibertini, M.; Giannini, E.; Morpurgo, A. F.; Maletinsky, P. Probing Magnetism in 2D Materials at the Nanoscale with Single-Spin Microscopy. *Science* **2019**, *364* (6444), 973–976.
- (10) Mamin, H. J.; Kim, M.; Sherwood, M. H.; Rettner, C. T.; Ohno, K.; Awschalom, D. D.; Rugar, D. Nanoscale Nuclear Magnetic Resonance with a Nitrogen-Vacancy Spin Sensor. *Science* **2013**, 339 (6119), 557–560.
- (11) Kim, D.; Ibrahim, M. I.; Foy, C.; Trusheim, M. E.; Han, R.; Englund, D. R. A CMOS-Integrated Quantum Sensor Based on Nitrogen-Vacancy Centres. *Nat. Electron.* **2019**, 2 (7), 284–289.
- (12) Ibrahim, M. I.; Foy, C.; Englund, D. R.; Han, R. 29.2 A Scalable Quantum Magnetometer in 65nm CMOS with Vector-Field Detection Capability. In 2019 IEEE International Solid-State Circuits Conference (ISSCC); IEEE, 2019; Vol. 2019-Feb, pp 458–461.
- (13) Gruber, A.; Dräbenstedt, A.; Tietz, C.; Fleury, L.; Wrachtrup, J.; von Borczyskowski, C. Scanning Confocal Optical Microscopy and Magnetic Resonance on Single Defect Centers. *Science* **1997**, *276* (5321), 2012–2014.
- (14) Doherty, M. W.; Manson, N. B.; Delaney, P.; Jelezko, F.; Wrachtrup, J.; Hollenberg, L. C. L. The Nitrogen-Vacancy Colour Centre in Diamond. *Phys. Rep.* **2013**, *528* (1), 1–45.
- (15) Balasubramanian, G.; Neumann, P.; Twitchen, D.; Markham, M.; Kolesov, R.; Mizuochi, N.; Isoya, J.; Achard, J.; Beck, J.; Tissler, J.; Jacques, V.; Hemmer, P. R.; Jelezko, F.; Wrachtrup, J. Ultralong Spin Coherence Time in Isotopically Engineered Diamond. *Nat. Mater.* **2009**, *8* (5), 383–387.
- (16) Toyli, D. M.; de las Casas, C. F.; Christle, D. J.; Dobrovitski, V. V.; Awschalom, D. D. Fluorescence Thermometry Enhanced by the Quantum Coherence of Single Spins in Diamond. *Proc. Natl. Acad. Sci. U. S. A.* **2013**, *110* (21), 8417–8421.
- (17) Rondin, L.; Tetienne, J. P.; Hingant, T.; Roch, J. F.; Maletinsky, P.; Jacques, V. Magnetometry with Nitrogen-Vacancy Defects in Diamond. *Rep. Prog. Phys.* **2014**, *77* (5), 056503.
- (18) Schirhagl, R.; Chang, K.; Loretz, M.; Degen, C. L. Nitrogen-Vacancy Centers in Diamond: Nanoscale Sensors for Physics and Biology. *Annu. Rev. Phys. Chem.* **2014**, *65* (1), 83–105.
- (19) Casola, F.; Van Der Sar, T.; Yacoby, A. Probing Condensed Matter Physics with Magnetometry Based on Nitrogen-Vacancy Centres in Diamond. *Nat. Rev. Mater.* **2018**, *3*, 17088.
- (20) Neumann, P.; Mizuochi, N.; Rempp, F.; Hemmer, P.; Watanabe, H.; Yamasaki, S.; Jacques, V.; Gaebel, T.; Jelezko, F.; Wrachtrup, J. Multipartite Entanglement Among Single Spins in Diamond. *Science* **2008**, *320* (5881), 1326–1329.
- (21) Maurer, P. C.; Kucsko, G.; Latta, C.; Jiang, L.; Yao, N. Y.; Bennett, S. D.; Pastawski, F.; Hunger, D.; Chisholm, N.; Markham, M.; Twitchen, D. J.; Cirac, J. I.; Lukin, M. D. Room-Temperature Quantum Bit Memory Exceeding One Second. *Science* **2012**, 336 (6086), 1283–1286.
- (22) Taminiau, T. H.; Cramer, J.; van der Sar, T.; Dobrovitski, V. V.; Hanson, R. Universal Control and Error Correction in Multi-Qubit Spin Registers in Diamond. *Nat. Nanotechnol.* **2014**, 9 (3), 171–176.
- (23) Kehayias, P.; Jarmola, A.; Mosavian, N.; Fescenko, I.; Benito, F. M.; Laraoui, A.; Smits, J.; Bougas, L.; Budker, D.; Neumann, A.; Brueck, S. R. J.; Acosta, V. M. Solution Nuclear Magnetic Resonance Spectroscopy on a Nanostructured Diamond Chip. *Nat. Commun.* 2017, *8*, 188.
- (24) Dolde, F.; Fedder, H.; Doherty, M. W.; Nöbauer, T.; Rempp, F.; Balasubramanian, G.; Wolf, T.; Reinhard, F.; Hollenberg, L. C. L.; Jelezko, F.; Wrachtrup, J. Electric-Field Sensing Using Single Diamond Spins. *Nat. Phys.* **2011**, *7* (6), 459–463.
- (25) Maze, J. R.; Stanwix, P. L.; Hodges, J. S.; Hong, S.; Taylor, J. M.; Cappellaro, P.; Jiang, L.; Dutt, M. V. G.; Togan, E.; Zibrov, A. S.; Yacoby, A.; Walsworth, R. L.; Lukin, M. D. Nanoscale Magnetic Sensing with an Individual Electronic Spin in Diamond. *Nature* **2008**, 455 (7213), 644–647.
- (26) Doherty, M. W.; Struzhkin, V. V.; Simpson, D. A.; McGuinness, L. P.; Meng, Y.; Stacey, A.; Karle, T. J.; Hemley, R. J.; Manson, N. B.; Hollenberg, L. C. L.; Prawer, S. Electronic Properties and Metrology

- Applications of the Diamond Center under Pressure. *Phys. Rev. Lett.* **2014**, *112* (4), 047601.
- (27) Trusheim, M. E.; Englund, D. Wide-Field Strain Imaging with Preferentially Aligned Nitrogen-Vacancy Centers in Polycrystalline Diamond. *New J. Phys.* **2016**, *18* (12), 123023.
- (28) Neumann, P.; Jakobi, I.; Dolde, F.; Burk, C.; Reuter, R.; Waldherr, G.; Honert, J.; Wolf, T.; Brunner, A.; Shim, J. H.; Suter, D.; Sumiya, H.; Isoya, J.; Wrachtrup, J. High-Precision Nanoscale Temperature Sensing Using Single Defects in Diamond. *Nano Lett.* **2013**, *13* (6), 2738–2742.
- (29) Kucsko, G.; Maurer, P. C.; Yao, N. Y.; Kubo, M.; Noh, H. J.; Lo, P. K.; Park, H.; Lukin, M. D. Nanometre-Scale Thermometry in a Living Cell. *Nature* **2013**, *500* (7460), 54–58.
- (30) Hopper, D.; Shulevitz, H.; Bassett, L. Spin Readout Techniques of the Nitrogen-Vacancy Center in Diamond. *Micromachines* **2018**, *9* (9), 437.
- (31) Shields, B. J.; Unterreithmeier, Q. P.; De Leon, N. P.; Park, H.; Lukin, M. D. Efficient Readout of a Single Spin State in Diamond via Spin-to-Charge Conversion. *Phys. Rev. Lett.* **2015**, *114* (13), 1–5.
- (32) Bourgeois, E.; Jarmola, A.; Siyushev, P.; Gulka, M.; Hruby, J.; Jelezko, F.; Budker, D.; Nesladek, M. Photoelectric Detection of Electron Spin Resonance of Nitrogen-Vacancy Centres in Diamond. *Nat. Commun.* **2015**, *6*, 8577.
- (33) Robledo, L.; Childress, L.; Bernien, H.; Hensen, B.; Alkemade, P. F. A.; Hanson, R. High-Fidelity Projective Read-out of a Solid-State Spin Quantum Register. *Nature* **2011**, *477* (7366), 574–578.
- (34) Jiang, L.; Hodges, J. S.; Maze, J. R.; Maurer, P.; Taylor, J. M.; Cory, D. G.; Hemmer, P. R.; Walsworth, R. L.; Yacoby, A.; Zibrov, A. S.; Lukin, M. D. Repetitive Readout of a Single Electronic Spin via Quantum Logic with Nuclear Spin Ancillae. *Science* **2009**, 326 (5950), 267–272.
- (35) Bougas, L.; Wilzewski, A.; Dumeige, Y.; Antypas, D.; Wu, T.; Wickenbrock, A.; Bourgeois, E.; Nesladek, M.; Clevenson, H.; Braje, D.; Englund, D.; Budker, D. On the Possibility of Miniature Diamond-Based Magnetometers Using Waveguide Geometries. *Micromachines* 2018, 9 (6), 276.
- (36) Bogdanov, S.; Shalaginov, M. Y.; Akimov, A.; Lagutchev, A. S.; Kapitanova, P.; Liu, J.; Woods, D.; Ferrera, M.; Belov, P.; Irudayaraj, J.; Boltasseva, A.; Shalaev, V. M. Electron Spin Contrast of Purcell-Enhanced Nitrogen-Vacancy Ensembles in Nanodiamonds. *Phys. Rev. B: Condens. Matter Mater. Phys.* **2017**, *96* (3), 035146.
- (37) Mouradian, S. L.; Schröder, T.; Poitras, C. B.; Li, L.; Goldstein, J.; Chen, E. H.; Walsh, M.; Cardenas, J.; Markham, M. L.; Twitchen, D. J.; Lipson, M.; Englund, D. Scalable Integration of Long-Lived Quantum Memories into a Photonic Circuit. *Phys. Rev. X* **2015**, *5* (3), na.
- (38) Siampour, H.; Kumar, S.; Bozhevolnyi, S. I. Nanofabrication of Plasmonic Circuits Containing Single Photon Sources. *ACS Photonics* **2017**, *4* (8), 1879–1884.
- (39) Bermúdez-Ureña, E.; Gonzalez-Ballestero, C.; Geiselmann, M.; Marty, R.; Radko, I. P.; Holmgaard, T.; Alaverdyan, Y.; Moreno, E.; García-Vidal, F. J.; Bozhevolnyi, S. I.; Quidant, R. Coupling of Individual Quantum Emitters to Channel Plasmons. *Nat. Commun.* 2015, 6, 7883.
- (40) Li, L.; Schröder, T.; Chen, E. H.; Walsh, M.; Bayn, I.; Goldstein, J.; Gaathon, O.; Trusheim, M. E.; Lu, M.; Mower, J.; Cotlet, M.; Markham, M. L.; Twitchen, D. J.; Englund, D. Coherent Spin Control of a Nanocavity-Enhanced Qubit in Diamond. *Nat. Commun.* **2015**, *6*, 6173.
- (41) Bhaskar, M. K.; Riedinger, R.; Machielse, B.; Levonian, D. S.; Nguyen, C. T.; Knall, E. N.; Park, H.; Englund, D.; Lončar, M.; Sukachev, D. D.; Lukin, M. D. Experimental Demonstration of Memory-Enhanced Quantum Communication. *Nature* **2020**, *580* (7801), 60–64.
- (42) Huck, A.; Andersen, U. L. Coupling Single Emitters to Quantum Plasmonic Circuits. *Nanophotonics* **2016**, *5* (3), 483–495.
- (43) Kinsey, N.; Ferrera, M.; Shalaev, V. M.; Boltasseva, A. Examining Nanophotonics for Integrated Hybrid Systems: A Review

- of Plasmonic Interconnects and Modulators Using Traditional and Alternative Materials [Invited]. J. Opt. Soc. Am. B 2015, 32 (1), 121.
- (44) Karaveli, S.; Gaathon, O.; Wolcott, A.; Sakakibara, R.; Shemesh, O. A.; Peterka, D. S.; Boyden, E. S.; Owen, J. S.; Yuste, R.; Englund, D. Modulation of Nitrogen Vacancy Charge State and Fluorescence in Nanodiamonds Using Electrochemical Potential. *Proc. Natl. Acad. Sci. U. S. A.* **2016**, *113* (15), 3938–3943.
- (45) Pfender, M.; Aslam, N.; Sumiya, H.; Onoda, S.; Neumann, P.; Isoya, J.; Meriles, C. A.; Wrachtrup, J. Nonvolatile Nuclear Spin Memory Enables Sensor-Unlimited Nanoscale Spectroscopy of Small Spin Clusters. *Nat. Commun.* **2017**, *8*, 834.
- (46) Ndukaife, J. C.; Kildishev, A. V.; Nnanna, A. G. A.; Shalaev, V. M.; Wereley, S. T.; Boltasseva, A. Long-Range and Rapid Transport of Individual Nano-Objects by a Hybrid Electrothermoplasmonic Nanotweezer. *Nat. Nanotechnol.* **2016**, *11* (1), 53–59.
- (47) Al-Baiaty, Z.; Cumming, B. P.; Gan, X.; Gu, M. Detection of the ODMR Signal of a Nitrogen Vacancy Centre in Nanodiamond in Propagating Surface Plasmons. J. Opt. (Bristol, U. K.) 2018, 20 (3), 035001
- (48) Siampour, H.; Kumar, S.; Davydov, V. A.; Kulikova, L. F.; Agafonov, V. N.; Bozhevolnyi, S. I. On-Chip Excitation of Single Germanium Vacancies in Nanodiamonds Embedded in Plasmonic Waveguides. *Light: Sci. Appl.* **2018**, *7*, 61.
- (49) Moreno, E.; Garcia-Vidal, F. J.; Rodrigo, S. G.; Martin-Moreno, L.; Bozhevolnyi, S. I. Channel Plasmon-Polaritons: Modal Shape, Dispersion, and Losses. *Opt. Lett.* **2006**, *31* (23), 3447.
- (50) Doherty, M. W.; Manson, N. B.; Delaney, P.; Jelezko, F.; Wrachtrup, J.; Hollenberg, L. C. L. The Nitrogen-Vacancy Colour Centre in Diamond. *Phys. Rep.* **2013**, 528 (1), 1–45.
- (51) Mohtashami, A.; Femius Koenderink, A. Suitability of Nanodiamond Nitrogen-Vacancy Centers for Spontaneous Emission Control Experiments. *New J. Phys.* **2013**, *15*, 043017.
- (52) Baburin, A. S.; Merzlikin, A. M.; Baryshev, A. V.; Ryzhikov, I. A.; Panfilov, Y. V.; Rodionov, I. A. Silver-Based Plasmonics: Golden Material Platform and Application Challenges [Invited]. *Opt. Mater. Express* **2019**, *9* (2), 611.
- (53) Haffner, C.; Chelladurai, D.; Fedoryshyn, Y.; Josten, A.; Baeuerle, B.; Heni, W.; Watanabe, T.; Cui, T.; Cheng, B.; Saha, S.; Elder, D. L.; Dalton, L. R.; Boltasseva, A.; Shalaev, V. M.; Kinsey, N.; Leuthold, J. Low-Loss Plasmon-Assisted Electro-Optic Modulator. *Nature* 2018, 556 (7702), 483–486.
- (54) Ono, M.; Hata, M.; Tsunekawa, M.; Nozaki, K.; Sumikura, H.; Chiba, H.; Notomi, M. Ultrafast and Energy-Efficient All-Optical Switching with Graphene-Loaded Deep-Subwavelength Plasmonic Waveguides. *Nat. Photonics* **2020**, *14* (1), 37–43.
- (55) Atikian, H. A.; Meesala, S.; Burek, M. J.; Sohn, Y.-I.; Israelian, J.; Patri, A. S.; Clarke, N.; Sipahigil, A.; Evans, R. E.; Sukachev, D. D.; Westervelt, R.; Lukin, M. D.; Lončar, M. Novel Fabrication of Diamond Nanophotonics Coupled to Single-Photon Detectors. *SPIE Newsroom* **2017**, *2*, 2–4.
- (56) Najafi, F.; Mower, J.; Harris, N. C.; Bellei, F.; Dane, A.; Lee, C.; Hu, X.; Kharel, P.; Marsili, F.; Assefa, S.; Berggren, K. K.; Englund, D. On-Chip Detection of Non-Classical Light by Scalable Integration of Single-Photon Detectors. *Nat. Commun.* **2015**, *6*, 5873.
- (57) Bogdanović, S.; Liddy, M. S. Z.; van Dam, S. B.; Coenen, L. C.; Fink, T.; Lončar, M.; Hanson, R. Robust Nano-Fabrication of an Integrated Platform for Spin Control in a Tunable Microcavity. *APL Photonics* **2017**, *2* (12), 126101.
- (58) Glenn, D. R.; Bucher, D. B.; Lee, J.; Lukin, M. D.; Park, H.; Walsworth, R. L. High-Resolution Magnetic Resonance Spectroscopy Using a Solid-State Spin Sensor. *Nature* **2018**, *555* (7696), 351–354.
- (59) DeVience, S. J.; Pham, L. M.; Lovchinsky, I.; Sushkov, A. O.; Bar-Gill, N.; Belthangady, C.; Casola, F.; Corbett, M.; Zhang, H.; Lukin, M.; Park, H.; Yacoby, A.; Walsworth, R. L. Nanoscale NMR Spectroscopy and Imaging of Multiple Nuclear Species. *Nat. Nanotechnol.* **2015**, *10* (2), 129–134.
- (60) Pham, L. M.; Le Sage, D.; Stanwix, P. L.; Yeung, T. K.; Glenn, D.; Trifonov, A.; Cappellaro, P.; Hemmer, P. R.; Lukin, M. D.; Park,

- H.; Yacoby, A.; Walsworth, R. L. Magnetic Field Imaging with Nitrogen-Vacancy Ensembles. New J. Phys. 2011, 13 (4), 045021.
- (61) Bayat, K.; Choy, J.; Farrokh Baroughi, M.; Meesala, S.; Loncar, M. Efficient, Uniform, and Large Area Microwave Magnetic Coupling to NV Centers in Diamond Using Double Split-Ring Resonators. *Nano Lett.* **2014**, *14* (3), 1208–1213.
- (62) Durán-Valdeiglesias, E.; Guerber, S.; Oser, D.; Roux, X. Le; Benedikovic, D.; Pérez-Galacho, D.; Vulliet, N.; Cremer, S.; Monfray, S.; Cassan, E.; Marris-Morini, D.; Baudot, C.; Boeuf, F.; Vivien, L.; Alonso-Ramos, C. Dual-Polarization Silicon Nitride Bragg Filters with Low Thermal Sensitivity. *Opt. Lett.* **2019**, *44* (18), 4578.
- (63) Bogdanov, S. I.; Makarova, O. A.; Xu, X.; Martin, Z. O.; Lagutchev, A. S.; Olinde, M.; Shah, D.; Chowdhury, S. N.; Gabidullin, A. R.; Ryzhikov, I. A.; Rodionov, I. A.; Kildishev, A. V.; Bozhevolnyi, S. I.; Boltasseva, A.; Shalaev, V. M.; Khurgin, J. B. Ultrafast Quantum Photonics Enabled by Coupling Plasmonic Nanocavities to Strongly Radiative Antennas. *Optica* **2020**, *7* (5), 463.
- (64) Schell, A. W.; Kewes, G.; Schröder, T.; Wolters, J.; Aichele, T.; Benson, O. A Scanning Probe-Based Pick-and-Place Procedure for Assembly of Integrated Quantum Optical Hybrid Devices. *Rev. Sci. Instrum.* **2011**, 82 (7), 073709.
- (65) Jaskula, J. C.; Shields, B. J.; Bauch, E.; Lukin, M. D.; Trifonov, A. S.; Walsworth, R. L. Improved Quantum Sensing with a Single Solid-State Spin via Spin-to-Charge Conversion. *Phys. Rev. Appl.* **2019**, *11* (6), 1.
- (66) Hopper, D. A.; Grote, R. R.; Parks, S. M.; Bassett, L. C. Amplified Sensitivity of Nitrogen-Vacancy Spins in Nanodiamonds Using All-Optical Charge Readout. *ACS Nano* **2018**, *12* (5), 4678–4686
- (67) O'Connor, D.; Ginzburg, P.; Rodríguez-Fortuño, F. J.; Wurtz, G. A.; Zayats, A. V. Spin-Orbit Coupling in Surface Plasmon Scattering by Nanostructures. *Nat. Commun.* **2014**, *5*, 5327.
- (68) Van Mechelen, T.; Jacob, Z. Universal Spin-Momentum Locking of Evanescent Waves. *Optica* **2016**, *3* (2), 118.
- (69) Togan, E.; Chu, Y.; Trifonov, A. S.; Jiang, L.; Maze, J.; Childress, L.; Dutt, M. V. G.; Sørensen, A. S.; Hemmer, P. R.; Zibrov, A. S.; Lukin, M. D. Quantum Entanglement between an Optical Photon and a Solid-State Spin Qubit. *Nature* **2010**, *466* (7307), 730–734.
- (70) Novotny, L.; Hecht, B. *Principles of Nano-Optics*; Cambridge University Press: Cambridge, 2006.